Supporting Information

^{57}Fe-enrichment effect on the composition and performance of Fe-based O_2-reduction electrocatalysts

Kathrin Ebner, Lingmei Ni, Viktoriia A. Saveleva, Benjamin P. Le Monnier, Adam H. Clark, Frank Krumeich , Maarten Nachtegaal, Jeremy S. Luterbacher, Ulrike I. Kramm, Thomas J. Schmidt, Juan Herranz

Experimental Methods

Material Preparation

The FeAc-based materials were prepared according to a synthesis procedure presented in a previous publication.[1] Briefly, PAN (Sigma-Aldrich, average molecular weight: 150 000 g·mol^{-1}) and Na_2CO_3 (Sigma-Aldrich, anhydrous, 99.999 % trace metal basis) in a weight ratio of 1:2 were stirred separately in dimethylformamide (DMF, Sigma-Aldrich, anhydrous 99.8 %) overnight at 80 °C. After mixing them at the same temperature for 1 h, Fe-phenanthroline was added in order to reach an initial Fe-content in the precursor mixture of 0.5 wt. % (unless otherwise specified). The Fe-complex was freshly prepared right before use by

combining Fe(II) acetate (standard: > 99.99 % trace metal basis, Sigma Aldrich; ^{57}Fe-enriched: > 95 % ^{57}Fe-isotope, PorLab; both stored inside a moisture- and O_2-free, Ar-filled glovebox) and 1,10-phenanthroline (Sigma-Aldrich, > 99 %) in a molar ratio of 1:5 in DMF.

After stirring for another hour, the solvent was partially evaporated and left to fully dry overnight in an oven at 110 °C. The precursor mixture was then ball milled in a sealed zirconia crucible (8 cycles at 300 rpm, 10 min per cycle with 5 min breaks in-between, zirconia balls (Ø 5mm), catalyst-to-balls weight ratio of 1:4.45), and a weighed amount of the resulting powder was transferred inside an alumina container and heat treated at 700 °C for 30 min in 5 % H_2 in Ar (100 mL·min^{-1}, Messer AG, 5.0). After acid washing overnight in 0.1 M $HClO_4$ (Merck Suprapur, 70 %) at room temperature, the catalyst was recovered by filtration, washed with abundant, ultrapure water (18.2 MΩ·cm, ELGA Purelab Ultra) and dried, to then undergo another heat treatment at 950 °C for 90 min in 5 % H_2 in Ar (100 mL·min^{-1}, Messer AG, 5.0). To produce the series of catalysts with varying extents of ^{57}Fe-enrichment, the ratio of ^{57}Fe-enriched and standard Fe(II)-acetate was varied to reach the desired ^{57}Fe-enrichment of each catalyst x_{Cat} according to Equation 1:

$$x_{cat} = \frac{m(^{57}Fe - prec.)}{m(Fe - prec.) + m(^{57}Fe - prec.)} * x_{^{57}Fe - prec.} + \frac{m(Fe - prec.)}{m(Fe - prec.) + m(^{57}Fe - prec.)} * 0.022 \quad (1)$$

where $m(^{57}Fe - prec.)$ and $m(Fe - prec.)$ were defined as the weighed amounts (i.e., masses) of the ^{57}Fe-enriched and standard Fe-precursor, respectively, while $x_{^{57}Fe - prec.}$ refers to the grade of ^{57}Fe-enrichment in the enriched precursor material as specified by the supplier (i.e., for FeAc, $x_{^{57}Fe - prec.}$= 95 % – *vide supra*). The factor 0.022 stems from the content of ^{57}Fe in the natural isotope mixture.[2]

The synthesis approach for the preparation of the porphyrin-based materials has been previously published[3] and relies on the homogeneous impregnation of 5,10,15,20-tetrakis(4-

methoxyphenyl)-21H,23H-porphine iron(III) chloride (FeTMPPCl, TriPorTech, purity > 96%, ^{57}FeTMPPCl with > 98% ^{57}Fe) on Ketjen Black EC-600JD carbon black (AzkoNobel). The series of catalysts with varying degrees of ^{57}Fe-enrichment (x_{cat} in Equation 1) studied herein were produced by varying the initial ratio of ^{57}Fe-enriched and standard porphyrin. After dissolution of this FeTMPPCl (mixture) in tetrahydrofuran (THF, in a ratio of 1.55 mg of porphyrin per mL of solvent), addition of the required carbon amount (see below) and 1 h of sonication, the solvent was removed with a rotary evaporator and the powder was fully dried in an oven at 80 °C overnight. The carbon and porphyrin quantities were chosen to reach an Fe-content of ≈ 1.7 wt. % in this dried precursor mixture; batch sizes varied from 1.2 to 2.7 g. The dried sample was subsequently subjected to a heat treatment in N_2-atmosphere in a split hinge furnace equipped with a quartz glass tube. The temperature was ramped at 5 K·min^{-1} until the final heat treatment temperature of 800 °C was reached and held for 30 min. Next, the sample was cooled down in N_2 followed by 1 h of acid washing in hydrochloric acid while sonicating. After filtering and washing with abundant amounts of water, the catalyst was dried at 80 °C in an oven.

In total, 7 samples were prepared and studied: FeAc-based catalysts with 2, 25, 49 and 95 % ^{57}Fe-enrichment and porphyrin-based catalysts containing 2, 54 and 98 % ^{57}Fe.

Electrochemical Testing

The materials' electrocatalytic activity towards the ORR was determined by the means of RDE voltammetry.[4] For the FeAc-based samples, the catalyst layers were prepared on a mirror-polished glassy carbon disk (5 mm diameter, HTW - Hochtemperatur-Werkstoffe GmbH) by dropcasting 21 µL of a catalyst ink as to reach a loading of 500 $\mu g_{catalyst} \cdot cm^{-2}$ (m_{Cat}). The catalyst ink was prepared with ultrapure water (18.2 MΩ·cm, ELGA Purelab Ultra),

isopropanol (Sigma-Aldrich, HPLC gradient grade, 99.9 %) and Nafion ionomer dispersion (5 %, Sigma-Aldrich), where the volume ratio of the first two components was 7:3 and the Nafion-to-catalyst-mass-ratio was 0.3, and then sonicated in cold water. The disk (embedded in a polytetrafluoroethylene (PTFE) RDE (Pine Research)) was then employed as the working electrode, while a gold mesh in a separate glass compartment served as the counter electrode. As a reference electrode, either a reversible hydrogen electrode (RHE) or silver/silver chloride (sat.) electrode (ALS Co., Ltd) calibrated against the RHE scale in the same electrolyte were used. All electrochemical testing was performed with a Bio-Logic SP-300 potentiostat at room temperature in 0.1 M perchloric acid electrolyte (Kanto Chemicals, 60%, Cica Reagent Ultrapure) saturated with N_2 (Messer AG, 5.0) or O_2 (Messer AG, 5.5). The catalyst-coated electrode was conditioned (25 cycles between 0.05 and 1.0 V vs. RHE at 50 mV·s^{-1}) in O_2-saturated electrolyte, before acquiring two polarization curves at 1600 rpm and 5 mV·s^{-1} employing the same potential window as above. After saturating with N_2 for 20 min, two cyclic voltammograms (CVs) were recorded to determine the capacitive current (i_{cap}) at 5 mV·s^{-1}. Potentiostatic electrochemical impedance spectroscopy (10 mV perturbation; 200 kHz to 0.1 Hz; 0.4 V vs. RHE) was employed to measure the resistance between working and reference electrode allowing for correcting ohmic losses. The ORR-activity at an iR-corrected potential of 0.8 vs. RHE was calculated by first determining the ORR-specific faradaic current density (i_F) as shown in Eq. 2 and then obtaining the kinetic current density (i_{kin} in A·g^{-1}) via Eq. 3.

$$i_F = i - i_{cap} \tag{2}$$

$$i_{kin} = \frac{1}{m_{cat}} * \frac{i_{lim} * i_F}{i_{lim} - i_F} \tag{3}$$

where i is the current density measured in O_2-saturated electrolyte and i_{lim} is the diffusion-limited current density (determined from the plateau of i_F at low potentials (0.05 V vs. RHE)).

The double-layer capacitance C in $F \cdot g^{-1}$ was obtained from cyclic voltammograms in N_2-saturated electrolyte, employing Eq. 4

$$C = \frac{\int_{V_1}^{V_2} i_{cap}(V)dV}{\frac{v}{V_2 - V_1}} \frac{1}{*m_{cat}} \quad (4)$$

where v is the scan rate and V_1 and V_2 represent the CVs' vertex potentials.

For the porphyrin-based materials, RDE-measurements were performed in 0.5 M H_2SO_4 electrolyte using a glassy carbon rod as the counter electrode and an Ag/AgCl (sat.) or $Hg/HgSO_4$ reference electrode pre-calibrated against the RHE scale. Inks were prepared by mixing 10 mL of ultra-pure water (Thermo Electron LED GmbH), 10 mL of ethanol (Sigma-Aldrich) and 781 µL of Nafion ionomer solution (5%, QUINTECH or Sigma Aldrich), and subsequently ultrasonicating 200 µL of the resulting solution with 1 mg of catalyst for 1 h, yielding an ink with a Nafion-to-catalyst mass ratio of 0.38. As described above, the catalyst layer was prepared on a rotating disk electrode (Pine research) equipped with a polished glassy carbon disk by dropcasting 5 µL of the ink, with a resulting catalyst loading of 0.13 $mg \cdot cm^{-2}$. Conditioning and capacitive current measurements were performed without rotation in N_2-saturated electrolyte; specifically, the catalyst was first cycled in a potential range of 0.0 to 0.9 V vs. RHE with a scan rate of 50 $mV \cdot s^{-1}$ (or 100 $mV \cdot s^{-1}$ for the fully ^{57}Fe-enriched catalyst) for 20 cycles, followed by two more cycles at scan rates of 100, 150, 200, and 300 $mV \cdot s^{-1}$. After fully saturating the electrolyte with oxygen, ORR polarization curves in the same potential range were acquired at a scan rate of 5 $mV \cdot s^{-1}$ and rotation speeds of

100, 200, 400, 576, 729 and 900 rpm. The activity was calculated at 0.8 V vs. RHE using Equations 2 and 3, whereby the potential was not iR-corrected for this sample series.

Material Characterization

To obtain information about the surface elemental composition of the materials, X-ray photoelectron spectroscopy (XPS) was measured in a VG Escalab 220iXL instrument (Thermo Fisher Scientific) operated at ≈ $2 \cdot 10^{-9}$ mbar. Spectra were recorded using focused monochromatized Al Kα radiation using dwell times of 50 ms. The pass energy accounted to 50 eV in 0.5 eV steps for survey spectra, while for spectra in a narrower energy range, 30 eV and 0.05 eV steps were used. Energy-calibration was subsequently performed by aligning the C1s peak to a binding energy of 284.6 eV. The parameters applied for the deconvolution of the N1s peak to obtain information on the pyridinic, nitrilic/Me-N_x-type, pyrrolic, graphitic and oxidized surface N-contents can be found in Ref. 5.

The Brunauer-Emmet-Teller (BET) equation was used in a relative pressure range from $0.02 \leq \frac{p}{p_0} \leq 0.12$ to calculate the total surface area of selected catalysts from N_2-physisorption measurements. The latter were performed with a Quantachrome Autosorb 1 instrument at 77 K after a weighed catalysts amount (≈ 10-20 mg) was outgassed overnight in a 9 mm bulb cell at 200 °C.

The bulk Fe-content of all FeAc-based catalysts and of the porphyrin-based material with 96 % ^{57}Fe-enrichment was determined by measuring inductively coupled plasma optical emission spectroscopy (ICP-OES) of the samples leached in aqua regia (consisting of a 3:1 volumetric mixture of HCl (37 %, for trace analysis) and HNO_3 (65 %, for analysis), both purchased from VWR), followed by evaporation of the acid to dryness and addition of 10 mL

of a 0.2 M solution of HNO_3 in ultrapure water. The filtrates were then analyzed using an Agilent 5110 instrument and quantified using the 259.940 nm spectral line. Standard solutions were prepared in the same matrix using a 1000 ppm stock solution (Sigma-Aldrich, certified reference material). For the other porphyrin-based catalysts (2 and 54 % ^{57}Fe-enriched), neutron activation analysis (NAA) at reactor BER-II of the Helmholtz-Zentrum in Berlin was the method of choice to obtain the bulk Fe-contents. Induced by neutron irradiation, the ^{58}Fe isotope is excited to ^{59}Fe and the content of iron is estimated from the decay scheme of this ^{59}Fe isotope in comparison to internal Fe-standards. Notably, in samples with a natural isotopic abundance like these Fe-standards, the ^{58}Fe-content accounts for 0.28 % of the isotopic inventory, whereas for the ^{57}Fe isotopically enriched samples the ^{58}Fe abundance changes. Based on this, a correction factor has to be determined in order to address the different content of $^{58/59}$Fe in ^{57}Fe-enriched samples versus the internal standard. In order to do so, the isotopic distributions of the non-enriched and of the ^{57}Fe-enriched FeTMPPCl were measured, and the derived relation of their corresponding $^{58}Fe_{Standard}/^{58}Fe_{sample}$ ratios were used to calculate the ^{58}Fe content for the sample with 54 % enrichment.

Scanning transmission electron microscopy (STEM) measurements were performed in an HD-2700CS dedicated STEM microscope (Hitachi) as well as on an FEI Talos F200X apparatus. The samples, which were prepared by dropcasting a suspension of the catalyst of interest in ethanol onto a perforated carbon foil supported on a copper grid (Agar Scientific, holey carbon film - copper, 400 mesh), were investigated using an acceleration potential of 200 kV (cold field emitter). Bright field (BF) as well as (high-angle) annular dark field ((HA)ADF) images were obtained, while the morphology was studied with secondary electron detection. Energy-dispersive X-ray (EDX) spectroscopy was employed to gather information

about the elemental composition in certain areas. For further details about the instruments, please refer to [6].

X-ray absorption spectra were recorded at the SuperXAS beamline of the Swiss Light Source (Villigen-PSI, Switzerland) which operated at 400 mA and 2.4 GeV.[7] A polychromatic beam resulting from the 2.9 T bending magnet was first collimated by a Si-coated mirror and subsequently monochromatized by a Si(111) channel-cut monochromator. Further focusing with a Rh-coated mirror resulted in a spot size at the sample position of 1 mm by 0.2 mm. Spectra of the samples pelletized with cellulose (Sigma-Aldrich) were collected at the Fe K-edge in either fluorescence- or transmission-detected quick-scanning mode.[7,8] A PIPS detector or 1 bar N_2-filled ionization chambers were employed as detectors for each configuration, respectively. An Fe-foil was employed as a reference and used for energy calibration by assigning the first maximum in its spectrum's first derivative to an energy of 7112 eV. Air sensitive samples (specifically the Fe-acetate precursors) were prepared inside the same Ar-filled glovebox in which the acetates were stored (*vide supra*) by placing the materials inside wax-sealed quartz capillaries and transported in airtight containers to avoid any oxygen contamination. Data treatment was performed using the Demeter software package[9] as well as ProXAS[10]. X-ray absorption near edge structure (XANES) spectra were normalized and subsequently fitted in the energy range spanning 20 eV below and 50 eV above the absorption edge by means of a linear combination of the spectra of Fe_3C[11] and of an Fe-based catalyst with its iron preponderantly in the form of Fe-N_x-sites (see sample 'Fe0.5' in Refs.[12] and [13]). Further, multivariate curve resolution (MCR) was employed applying the following constraints: non-negativity of the component spectra as well as of the component contributions, and the sum of all components' contributions equals unity. After normalizing and converting to the *k*-space, the extended X-ray absorption fine

structure (EXAFS) spectra were Fourier-transformed (FT) from 2.55 to 10 $Å^{-1}$ and the resulting FT-EXAFS were fitted in a range of 1 to 3 Å. To do so, theoretical scattering paths were calculated via FEFF using the structures of Fe_2O_3 and Fe_3C as input[14] and additionally a single oxidic Fe-Fe scattering path at 2.52 Å was generated.[15] The required amplitude reduction factors were obtained by fitting the corresponding Fe-foil reference spectra and amounted to 0.70 – 0.71.

Mössbauer spectroscopic measurements were carried out in transmission mode at room temperature. To do so, 80-100 mg of sample were placed in a PTFE holder (diameter: 15 mm), fixed by adhesive tape (Tesafilm®, Tesa) and irradiated by γ-rays provided by a 50 mCi Co/Rh source. The obtained data was analyzed with the Recoil software and fitted using the components displayed in Table S1, assuming Lorentzian-shaped signals for all Fe-sites. The relative absorption areas of the different species were corrected by the respective Lamb-Mössbauer factors (LMF) as determined by Sougrati et al. in [16] and listed in Table S2. Note that these LMFs were inferred from Mössbauer spectroscopic measurements of Fe-N-C-catalysts that had been synthesized using a preparation route that uses different precursors and a significantly higher pyrolysis temperature (1050 °C) than those of the catalysts featured in this study and thus herein we assume that these differences do not affect the values of these LMFs.

Raman spectra were acquired using a Labram HR800 Raman microscope (Horiba-Jobin Yvon) with a He−Ne excitation laser (632.8 nm). The hole and slit of the confocal system were fixed at 1000 and 100 µm, respectively. The laser was focused on the sample using a 50× (numerical aperture 0.55) objective, which produced a laser spot of ≈ 4 µm diameter with an estimated sampling depth of ≈ 2 µm.[17] The probed sample spot was continuously focused during the experiment using an autofocus function. Every spectrum was the

average of 15 acquisitions. The fitting of the Raman spectra was done by applying 4 Lorentzian profiles, whereby the constraints of band positions and widths are shown in Table S3. At least 3 different spots have been studied for every catalyst and their corresponding peak areas have been averaged to obtain the spectra plotted.

Thermogravimetric analyses were performed on a Netsch 449C instrument using Al_2O_3 crucibles. The Fe-porphyrins were measured in pristine condition, whereas Fe-phenanthroline, which was prepared in ethanolic solution, was first impregnated on Black Pearls 2000 carbon. This was achieved by mixing 70 wt.% of carbon with 30 wt.% Fe-phenanthroline, stirring for 30 min and evaporating the solvent at 50°C. The dried powder was ground in a mortar. After placing a weighed amount of the resulting powder in the crucible, the sample was heated in a 60 cm^3 flow of He with 5 % H_2 with heating steps as follows: from 40 to 150 °C at 10 °C/min followed by 1 h isothermal step; from 150 to 700 °C at 5 °C/min with a subsequent 1 h isothermal step; from 700 to 900 °C at 5 °C/min and lastely a cooling step till room temperature at 20 °C/min. The porphyrins were analyzed in inert atmosphere with a 5 °C/min heating ramp and an isothermal hold at 800°C to resemble synthesis conditions. The heating profiles are further displayed in Fig. S22. In all data the buoyancy force was corrected by measuring in the same conditions an empty crucible (baseline).

Supplementary Results & Discussion

Activity and composition of porphyrin-based catalysts

The degree of ^{57}Fe-enrichment for a series of porphyrin-based catalysts (see experimental section for details on the synthesis) was modified between 2 % (natural abundance) and 98 % (fully enriched sample), while the Fe-content in the precursor mixture was kept constant at 1.7 wt. %. The resulting materials were again tested for their ORR-activity using RDE-voltammetry (see above for details) and the corresponding results are displayed in Fig. S13a (with representative polarization curves plotted in Fig. S14). Similar to what was observed for the FeAc-derived materials, a systematic change of the ORR-activity with ^{57}Fe-enrichment extent was also detected for these porphyrin-based catalysts – however, in this case the trend was reversed and a higher content of ^{57}Fe led to a significant improvement of the ORR-activity (i.e. from ≈ 0.2 to ≈ 0.6 $A \cdot g^{-1}$ at 0.8 V vs. RHE upon increasing the ^{57}Fe-enrichment degree from 2 to 98 %). As it was already the case for the FeAc-based samples, the differences in the catalysts' final Fe-contents (ranging from ≈ 0.7 to 1.0 wt. %, cf. Fig. S15a) and double layer capacitances (≈ 33 to 46 $F \cdot g^{-1}$, see Fig. 15b) can be excluded as the dominant causes for the observed trend, since the ORR-activity vs. ^{57}Fe-enrichment correlation remained valid upon normalizing the catalytic activity with regard to these variables (cf. Figs. S13b and S16, respectively).

To shed light on this behavior, we again employed room temperature MS to elucidate the composition of these four porphyrin-based catalysts. Fig. S17 and Table S1 display the corresponding fits and derived parameters, which are partially different when compared to the FeAc-based sample series to allow the best possible fits of the acquired spectra (see the visual comparison of the isomer shift and quadrupole splitting values in Fig. S18). Specifically, while all deconvoluted spectra (cf. Fig. S17) feature again three doublets assigned to Fe-N_x-

sites, only doublets D1 and D2* seemed to feature similar iron signatures (note that we have assigned the latter D2* doublet to the same kind of site as D2, if marking it with a '*' to highlight its wider distribution of isomer shift and quadrupole splitting, – cf. Table S1). Complementarily, the D3 component observed in FeAc-based catalysts was absent and instead another doublet (D4) was found in these porphyrin-based samples. Moreover, the latter are devoid of the sextets featured by the FeAc-based catalysts that were previously assigned to α-Fe and Fe_3C. Instead, at the room temperature at which these MS measurements were performed, the superparamagnetic iron at the origin of the spectral singlet contribution was the only detectable inorganic iron phase present in this porphyrin-based sample series. Interestingly, some compositional trends are observable for the three catalysts displayed in Fig. S19: their LMF-corrected relative D1 absorption areas increase with ^{57}Fe-enrichment, which led to a concomitant decrease of D2* and D4 that was accompanied by an increase of the singlet's content. Hence, an increase of cumulative inorganic Fe content with ^{57}Fe-enrichment is observed for both catalyst series. Nonetheless, the contribution of the inorganic side phase is minor (< 10 %), and the majority of iron atoms can be found in various Fe-N_x-environments.

Supplementary Tables and Figures

Table S1: Summary of the isomer shift (δ_{ISO}), quadrupole splitting (ΔE_Q) and full width at half maximum (fwhm) values derived from the fitting of the Mössbauer spectra recorded on the FeAc-derived catalysts with 25, 49 or 95 % ^{57}Fe-enrichment (referred to as FeAc), and on the porphyrin-based materials with 2, 54 or 98 % ^{57}Fe-enrichment (referred to as Porph), along with their corresponding assignment to different Fe-species.[18,19] Note that the "♦" symbols denote parameter values that were fixed for the fitting of the corresponding component. The reported error values correspond to a 95 % confidence interval.

Sites		FeAc, 25%	FeAc, 49 %	FeAc, 95 %	Porph, 2%	Porph, 54%	Porph, 98%	Assignment[18,19]
Sing	δiso / mm·s^{-1}	-0.11 ± 0.02	-0.09 ± 0.02	-0.09 ± 0.00	-0.14 ± 0.12	-0.14 ±0.05	-0.07 ± 0.03	Superparamagnetic iron
	fwhm / mm·s^{-1}	0.4♦	0.4♦	0.4♦	0.4♦	0.4♦	0.4♦	
D1	δiso / mm·s^{-1}	0.31 ± 0.01	0.36 ±0.01	0.25 ± 0.01	0.29 ±0.03	0.24 ±0.03	0.31 ± 0.03	$Fe^{II}N_4$, low spin, Fe/FeO Clusters [60]
	ΔE_Q / mm·s^{-1}	1.30 ± 0.04	1.01 ± 0.02	1.19 ± 0.02	1.10 ± 0.06	1.13 ± 0.06	1.04 ± 0.06	
	fwhm / mm·s^{-1}	0.7♦	0.7♦	0.7♦	0.79 ± 0.09	0.79♦	0.79♦	
D2 and D2*	δiso / mm·s^{-1}	0.36♦	0.35♦	0.36♦	0.28 ± 0.10	0.34 ± 0.08	0.45 ± 0.10	D2 (FeAc): $Fe^{II}N_4$, intermediate spin D2*(Porph): $Fe^{II}N_4$,intermediate spin
	ΔE_Q / mm·s^{-1}	2.52 ± 0.07	2.36 ± 0.03	2.47♦	2.89 ± 0.23	2.71 ± 0.10	2.96 ± 0.13	
	fwhm / mm·s^{-1}	0.7♦	0.7♦	0.7♦	0.78 ± 0.32	0.77♦	0.77♦	
D3	δiso / mm·s^{-1}	1.08 ± 0.03	0.92 ± 0.04	1.10 ± 0.02	-	-	-	$Fe^{II}N_4$, high spin
	ΔE_Q / mm·s^{-1}	1.94 ± 0.08	2.13 ± 0.07	1.78 ± 0.03	-	-	-	
	fwhm / mm·s^{-1}	0.7♦	0.7♦	0.7♦	-	-	-	
D4	δiso / mm·s^{-1}	-	-	-	0.08 ± 0.07	-0.01 ± 0.09	0.01 ± 0.12	$Fe^{III}N_4$, intermediate spin⊥
	ΔE_Q / mm·s^{-1}	-	-	-	3.17 ± 0.14	2.72 ± 0.16	3.13 ± 0.18	
	fwhm / mm·s^{-1}	-	-	-	0.6♦	0.6♦	0.6♦	
Sext1	δiso / mm·s^{-1}	0.20 ± 0.00	0.19 ± 0.00	0.20 ± 0.00	-	-	-	iron carbide
	ΔE_Q / mm·s^{-1}	0♦	0♦	0♦	-	-	-	
	H / mm·s^{-1}	20.76 ± 0.03	20.66 ± 0.01	20.77 ± 0.01	-	-	-	
	fwhm / mm·s^{-1}	0.40 ± 0.01	0.38 ± 0.01	0.38 ± 0.00	-	-	-	
Sext2	δiso / mm·s^{-1}	-0.04 ± 0.05	-0.01 ± 0.00	0.01 ± 0.01	-	-	-	alpha iron
	ΔE_Q / mm·s^{-1}	0♦	0♦	0♦	-	-	-	
	H / mm·s^{-1}	32.96 ± 0.47	32.97 ± 0.04	32.89 ± 0.06	-	-	-	
	fwhm / mm·s^{-1}	0.25 ± 0.12	0.27 ± 0.01	0.31 ± 0.03	-	-	-	

⊥ Comment on the tentative assignment of D4: if only isomer shift is considered, both ferryl high spin and ferric intermediate spin sites would be possible; however, since the quadrupole splitting is quite large, a ferric intermediate spin state seems more likely, as the unequal distribution of spins in the d-orbitals is a main contributor to the electric field gradient and the resulting ΔE_Q value.

Table S2: Lamb-Mössbauer factors[16] (LMFs) used for correcting the relative absorption areas derived from the fitting of the acquired MS spectra.

Sites	LMF
Sing	0.77
D1	0.46
D2	0.52
D2*[1]	0.52
D3[2]	0.49
D4[1]	0.52
Sext1	0.77
Sext2	0.67

[1]Since the Mössbauer parameters of D2* and D4 are similar to those of D2 in Ref. [16], the same Lamb-Mössbauer factor is assumed for these sites.
[2]Since no LMF value was specified for this doublet component in Ref. [16], an average of the values reported in the same study for doublets D1 and D2 was assumed.

Table S3. Description and constrains in the wave number positions and widths of the bands considered to fit the recorded first order Raman spectra of the FeAc-based Fe-N-C catalysts.

Band	Position constraints / cm^{-1}	Full width at half maximum constraints / cm^{-1}	Description	Ref.
D	1331 – 1333	148 – 160	Planar motion of sp^2 – hybridized carbon in an ideal graphene layer, graphite	20
G	1591 – 1594	66 – 76	From carbon atoms close to the edge of a graphene sheet, defect.	20,21
Am	1490 – 1500	170 – 180	Amorphous carbon originated from organic molecules, molecular fragments or functional groups	22
P	1205	200 - 225	sp^3 carbon, polyenes, ionic impurities	22

Table S4: Structural parameters derived from the best fits of the Fourier-transformed EXAFS spectra of the FeAc-based samples synthesized with 2 to 95 % 57Fe-enrichment, where N refers to the coordination number, R is the first-shell bond scattering distance, σ2 is the pseudo Debye-Waller factor, ΔE0 refers to the energy shift, and the R-factor is a statistic parameter for which values below 0.02 indicate a good quality EXAFS fit.23 The reported parameters and errors were obtained from fitting with the Artemis software.9

^{57}Fe-Enrich. / %	Scatterer	N	R / Å	^{2} / Å^{2}	ΔE_0 / eV	R-factor
2	Fe-O	4.5 ± 0.1	1.98 ± 0.01	0.012	0.0 ± 0.9	0.001
	Fe-Fe	1.5 ± 0.1	2.61 ± 0.01	0.009	0.0 ± 0.9	
25	Fe-O	4.1 ± 0.3	1.98 ± 0.02	0.012	-0.3 ± 2.4	0.005
	Fe-Fe	2.9 ± 0.2	2.66 ± 0.03	0.009	-0.3 ± 2.4	
49	Fe-O	2.8 ± 1.1	1.96 ± 0.04	0.012	-2.8	0.028
	Fe-Fe	6.7 ± 0.6	2.57 ± 0.02	0.009	-2.8	
>95	Fe-O	3.5 ± 0.7	1.96 ± 0.05	0.012	-2.8 ± 6.2	0.011
	Fe-Fe	5.5 ± 0.4	2.63 ± 0.07	0.009	-2.8 ± 6.2	

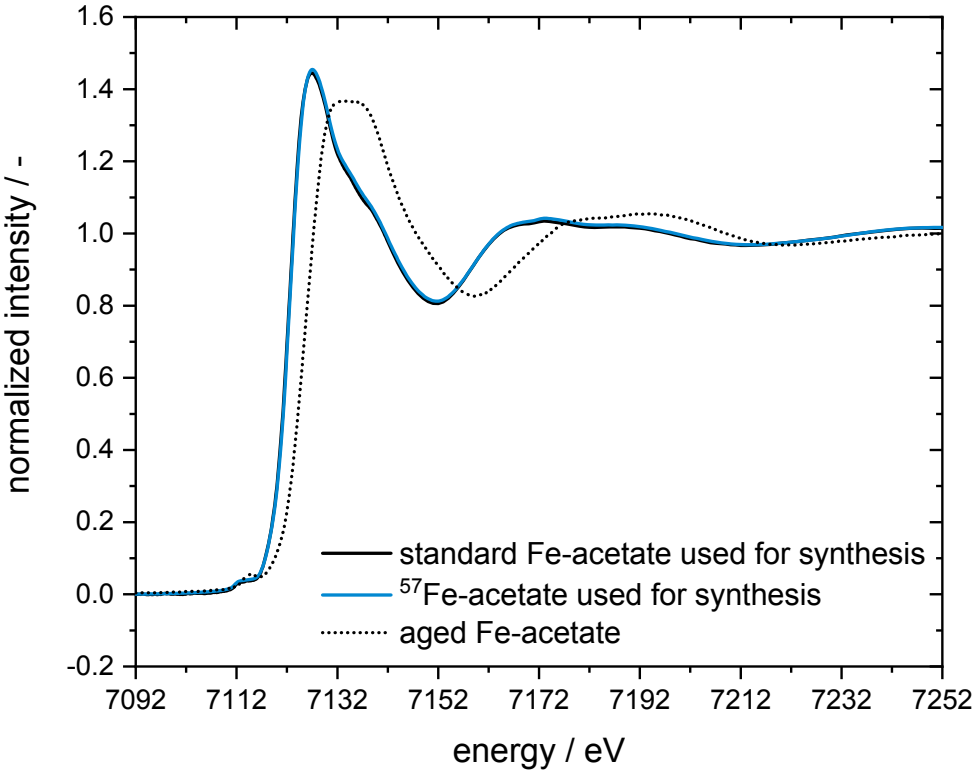

Figure S1: XANES spectra of the ^{57}Fe-enriched and standard Fe-acetate precursors used for the FeAc-based synthesis, as well as that of an aged Fe-acetate sample (left in contact with atmospheric air for several weeks).

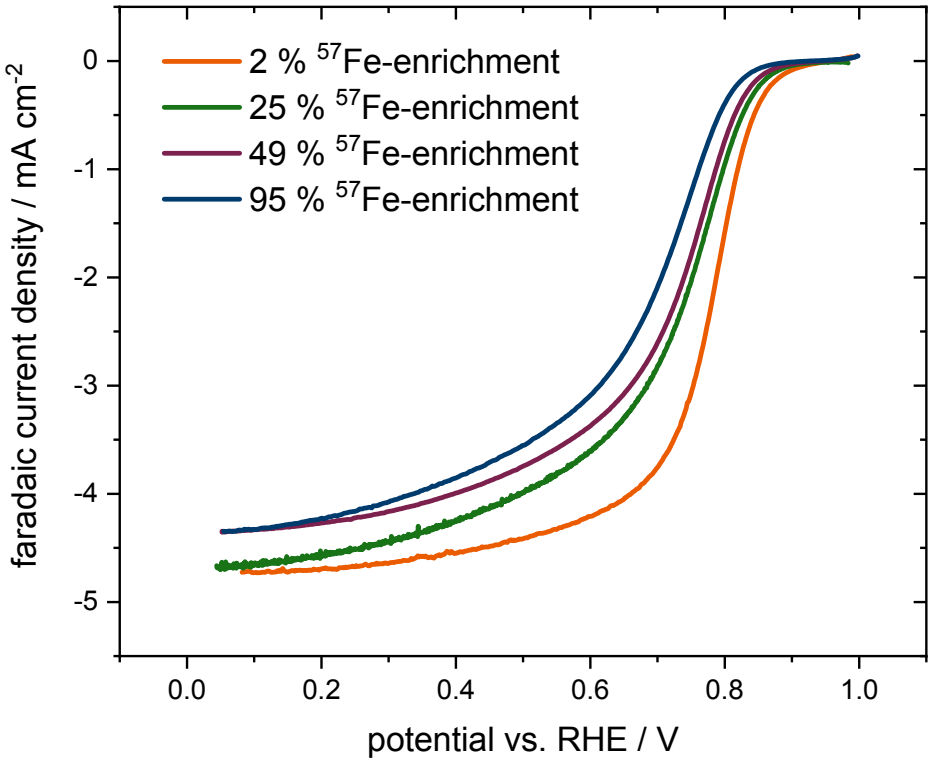

Figure S2: Capacitively- and ohmically-corrected polarization curves measured for the FeAc-based samples in O_2-saturated 0.1 M $HClO_4$ electrolyte at 1600 rpm, 5 mV·s^{-1} and with a

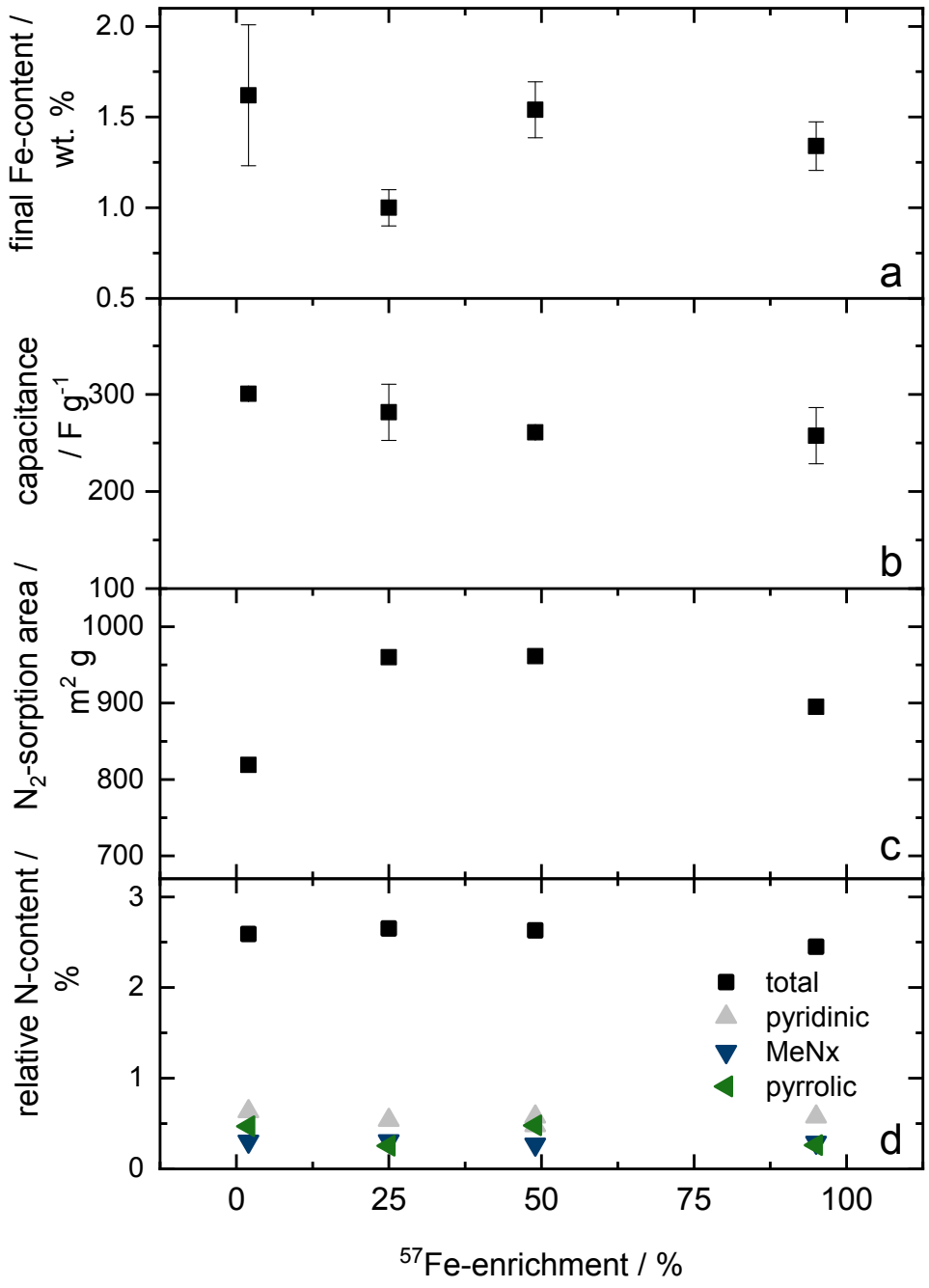

Figure S3: Physicochemical properties of the FeAc-based catalyst series as a function of their degree of ^{57}Fe-enrichment: final Fe-content measured by ICP-OES (a), double layer capacitance derived from cyclic voltammetry measurements in N_2-saturated 0.1 M $HClO_4$ (b), N_2-sorption area determined by BET analysis (c), and surface nitrogen content obtained from XPS measurements, alongside the relative N-content of pyridinic, MeNx and pyrrolic N-sites derived from the deconvoluted XPS spectra using the fitting constraints specified in Ref. 5.

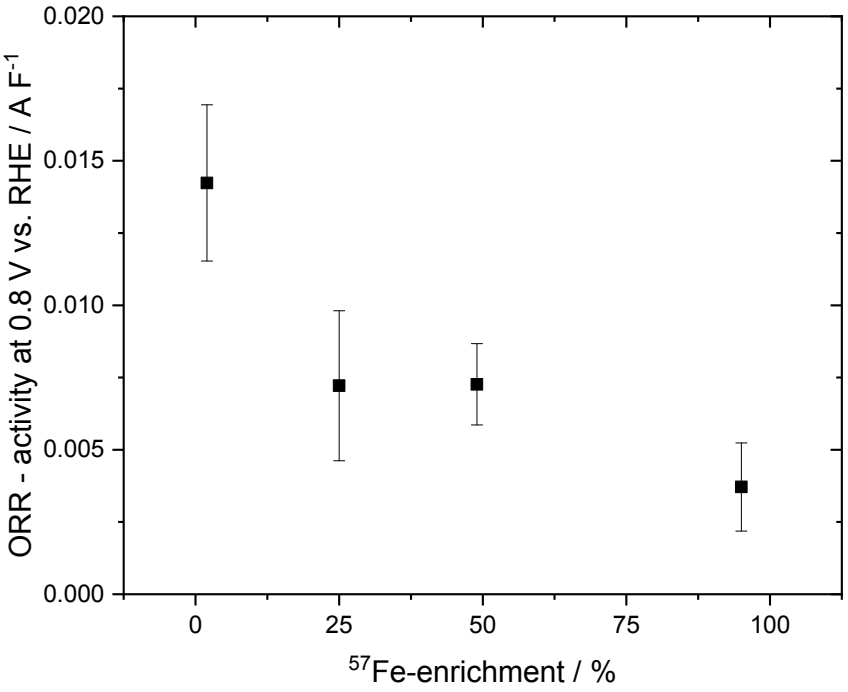

Figure S4: Effect of the degree of ^{57}Fe-enrichment of the four FeAc-based catalysts on their electrochemical activity towards the ORR, expressed as the kinetic current at an iR-corrected potential of 0.8 V vs. RHE and normalized with regards to their double layer capacitance in cyclic voltammetry measurements in N_2-saturated 0.1 M $HClO_4$ electrolyte.

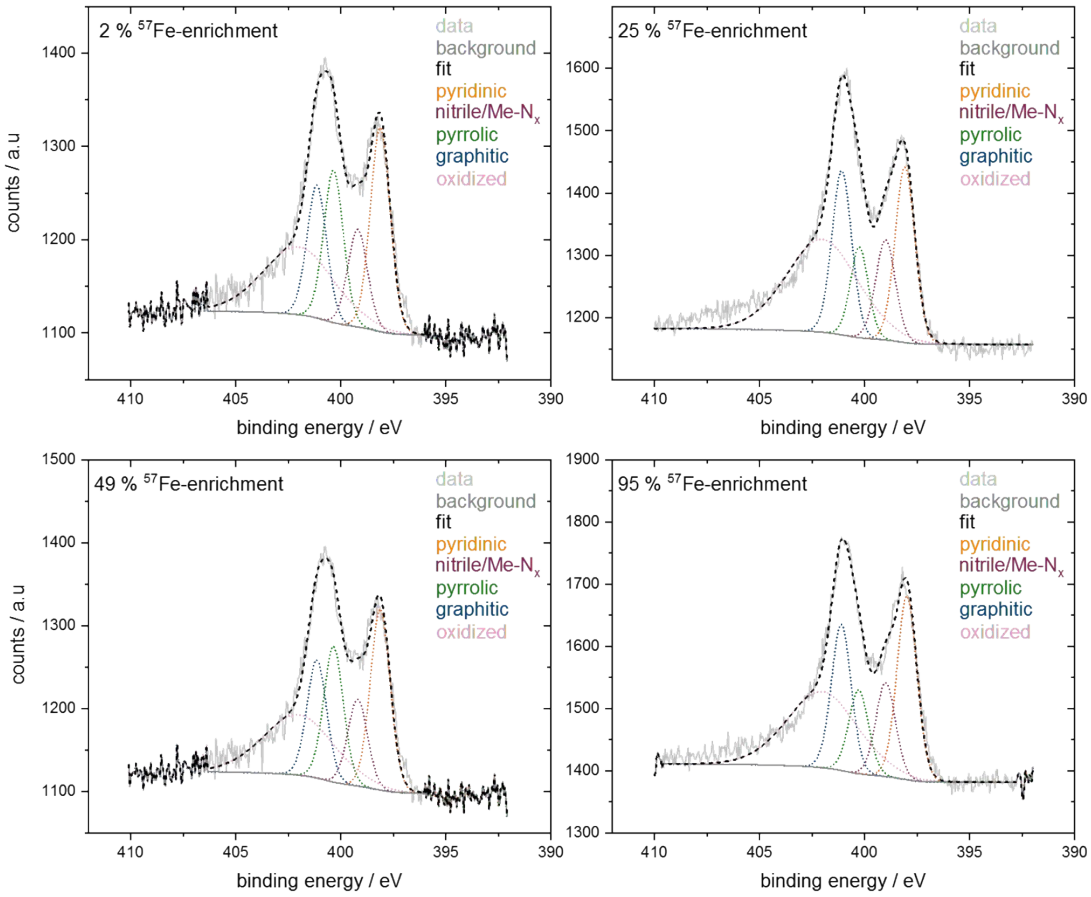

Figure S5: deconvoluted N1s XPS spectra of the FeAc-based catalysts synthesized with 2 to

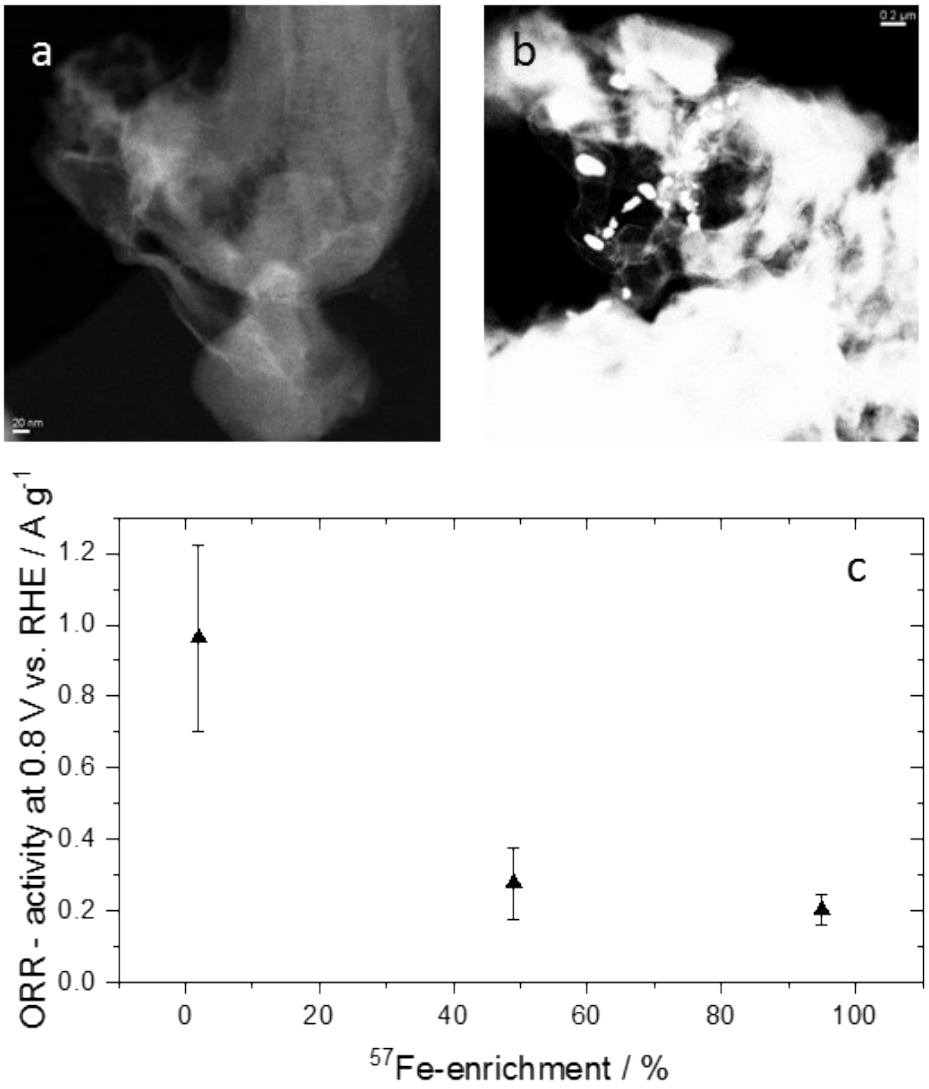

Figure S6: STEM images of two FeAc-based catalysts prepared with an equivalent initial iron content of 0.1 wt. % without any ^{57}Fe-enrichment (a) or with a fully enriched ^{57}Fe-precursor (b). The technique's Z-contrast reveals the presence of a significant amount of Fe-based agglomerates in the ^{57}Fe-enriched sample. Effect of the degree of ^{57}Fe-enrichment on the electrochemical activity of the materials towards the ORR (c).

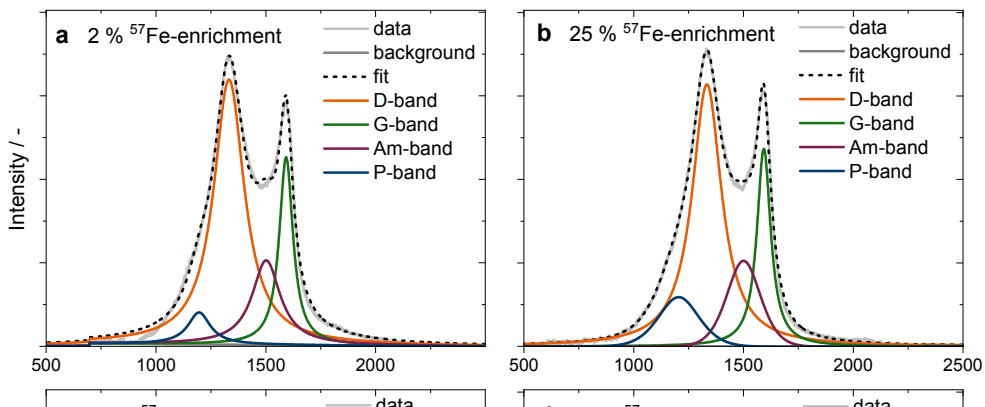

Figure S7: Deconvoluted Raman spectra of the FeAc-based catalysts synthesized with 0 (a), 25 (b), 50 (c) or 100 % (d) ^{57}Fe-enrichment, as well as the corresponding ratio between D- and G-bands as a function of the ^{57}Fe-enrichment extent (e).

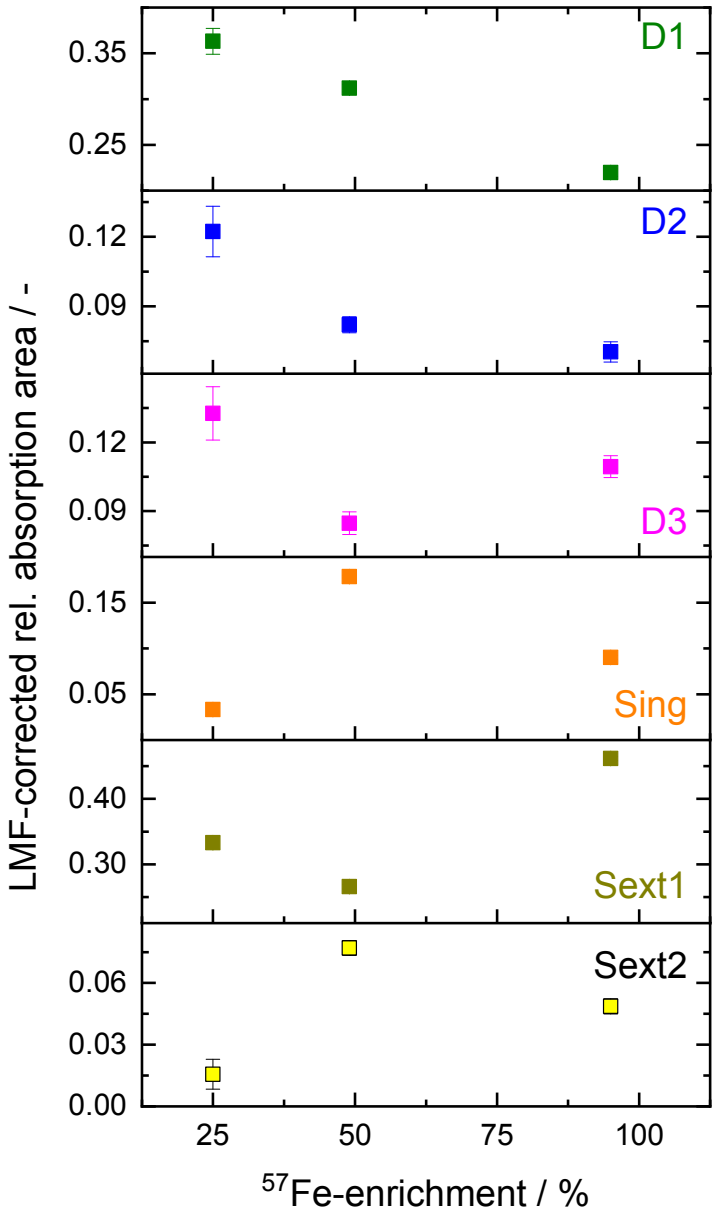

Figure S8: Lamb Mössbauer factors' (LMF-) corrected relative absorption areas of the different components identified in the deconvoluted Mösbauer spectra of the FeAc-based catalysts with different ^{57}Fe-enrichment extents, plotted individually for each fitting components and as a function of this degree of ^{57}Fe-enrichment.

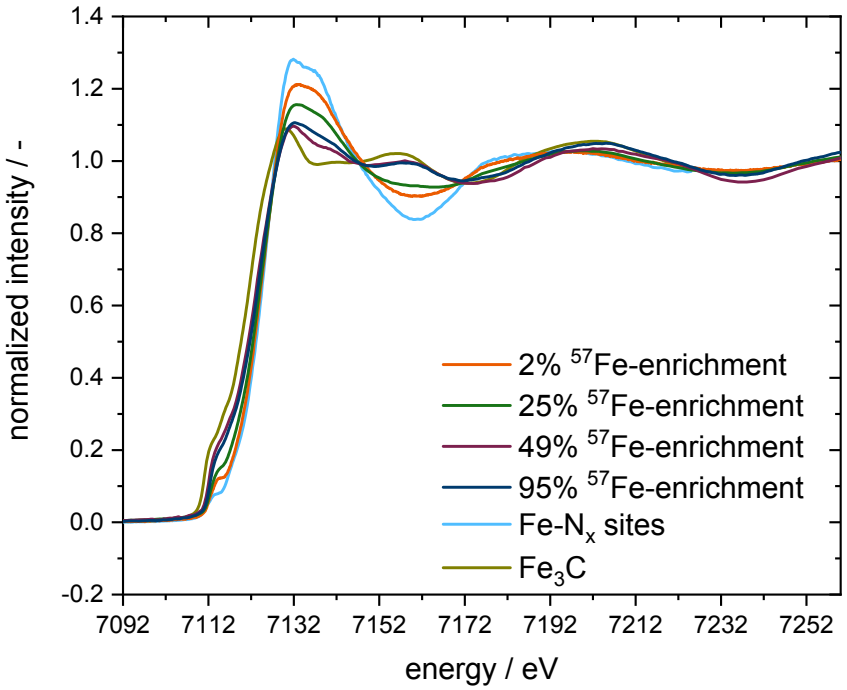

Figure S9: XANES spectra of the four catalysts derived from the FeAc-based synthesis, alongside the components used for linear combination fitting. Note that the spectrum of the FeNx-sites corresponds to that of the Fe0.5 sample in Ref. 12.

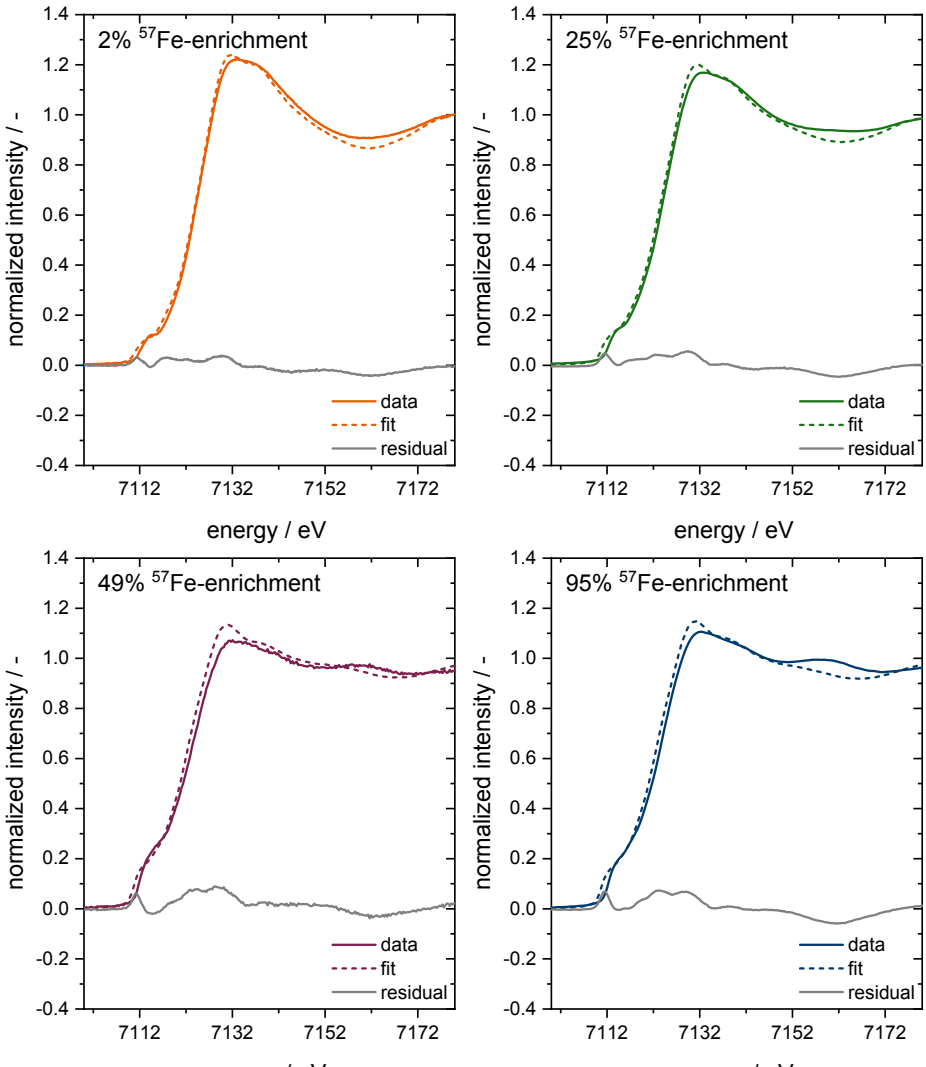

Figure S10: Visualized linear combination fits of the XANES spectra of the FeAc-based catalysts synthesized with 2 to 95 % ^{57}Fe-enrichment.

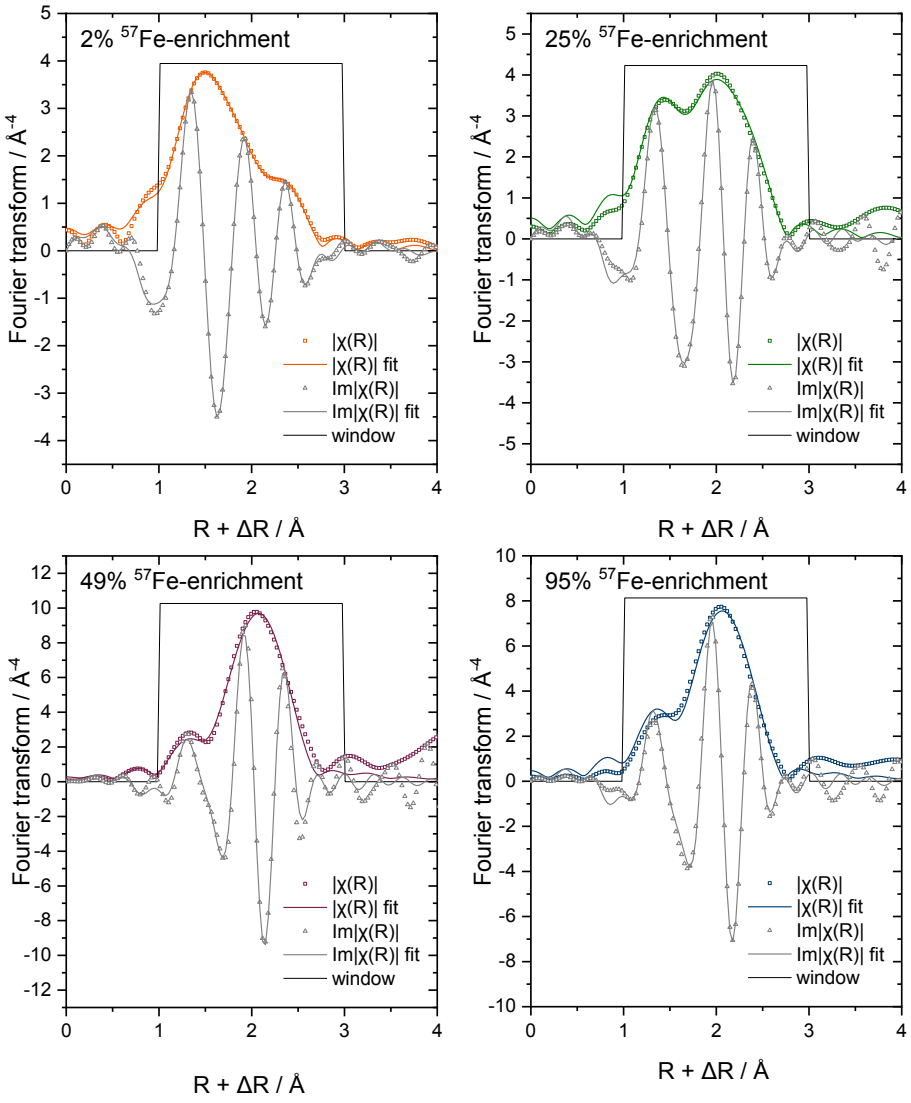

Figure S11: EXAFS fits for the FeAc-based catalysts synthesized with 2 to 95 % ^{57}Fe-enrichment.

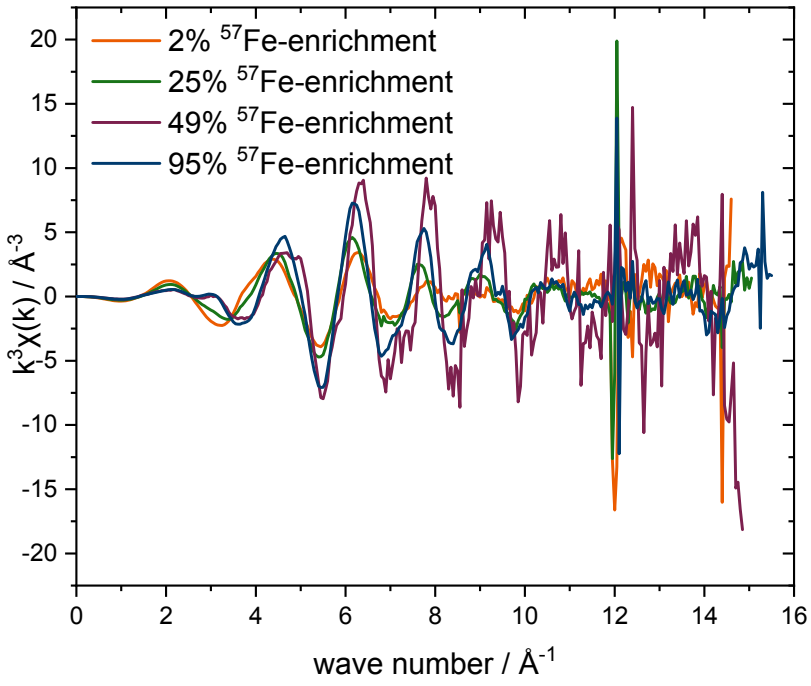

Figure S12: k^3-weighed EXAFS spectra as a function of the wave number for the FeAc-based catalysts synthesized with 2 to 95 % ^{57}Fe-enrichment.

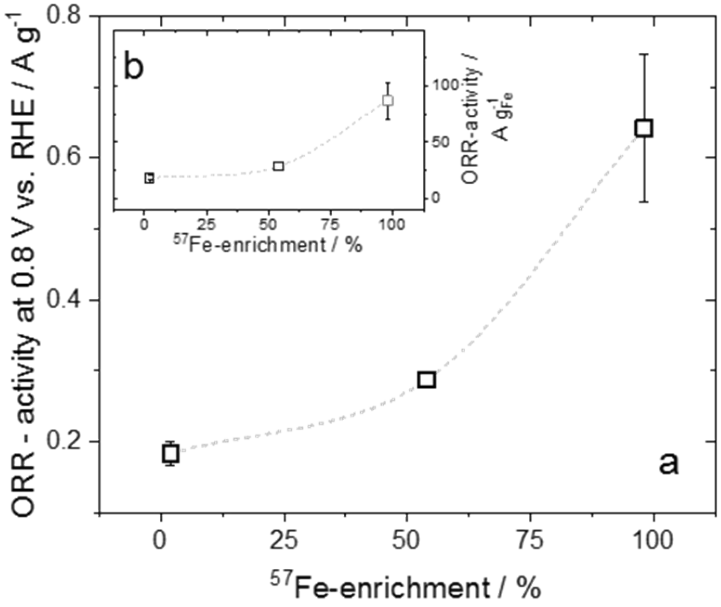

Figure S13: Effect of the degree of ^{57}Fe-enrichment of three Fe-porphyrin based catalysts made with an initial iron content of 1.7 wt. % Fe on their electrochemical activity towards the ORR, expressed as the kinetic current at a potential of 0.8 V vs. RHE normalized with regards to the catalysts' overall mass (a) and to their final Fe-content (b). Dashed lines are mere guides to the eye.

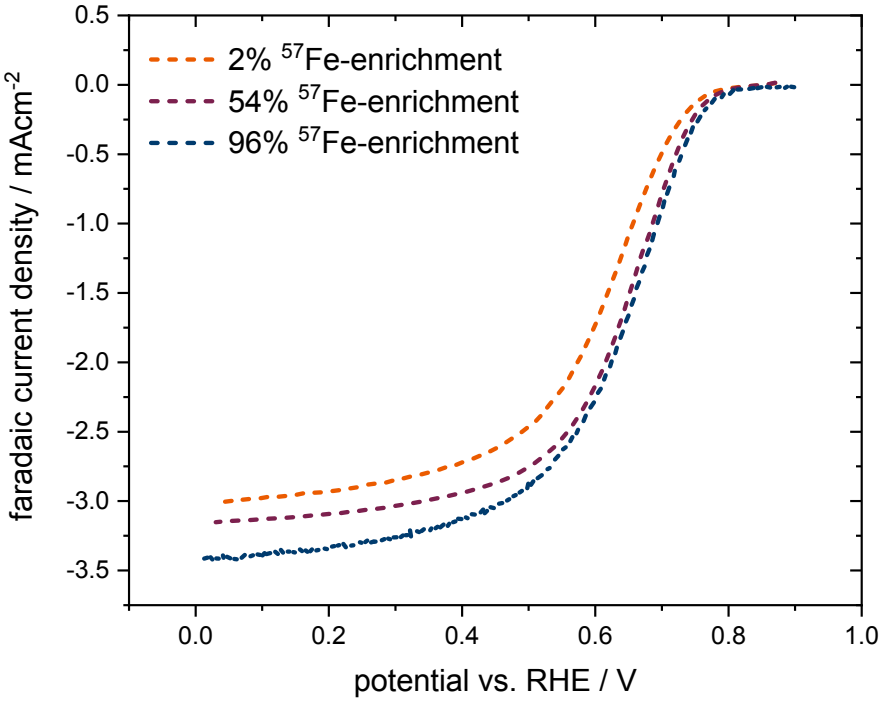

Figure S14: Capacitively- and ohmically-corrected faradaic currents measured for the porphyrin-based samples in O_2-saturated 0.1 M $HClO_4$ electrolyte at 1600 rpm.

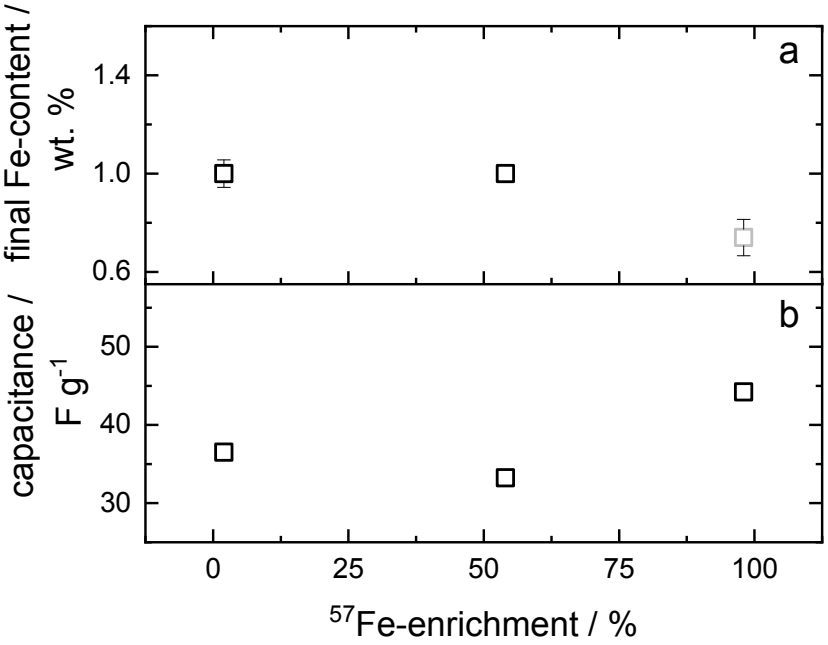

Figure S15: Physicochemical properties of the porphyrin-based catalyst series as a function of their degree of ^{57}Fe-enrichment: final Fe-content measured by ICP-OES (a) and double layer capacitance derived from cyclic voltammetry measurements in N_2-saturated electrolyte (b).

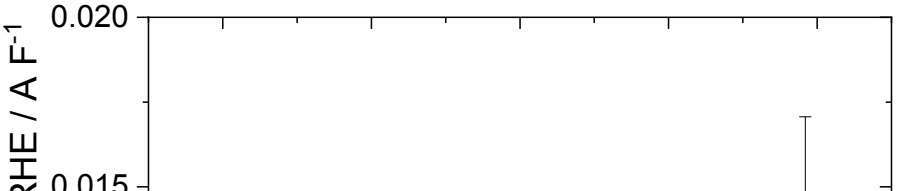

Figure S16: Effect of the degree of ^{57}Fe-enrichment of the four porphyrin-based catalysts on their electrochemical activity towards the ORR, expressed as the kinetic current at a potential of 0.8 V vs. RHE and normalized with regards to their capacitance.

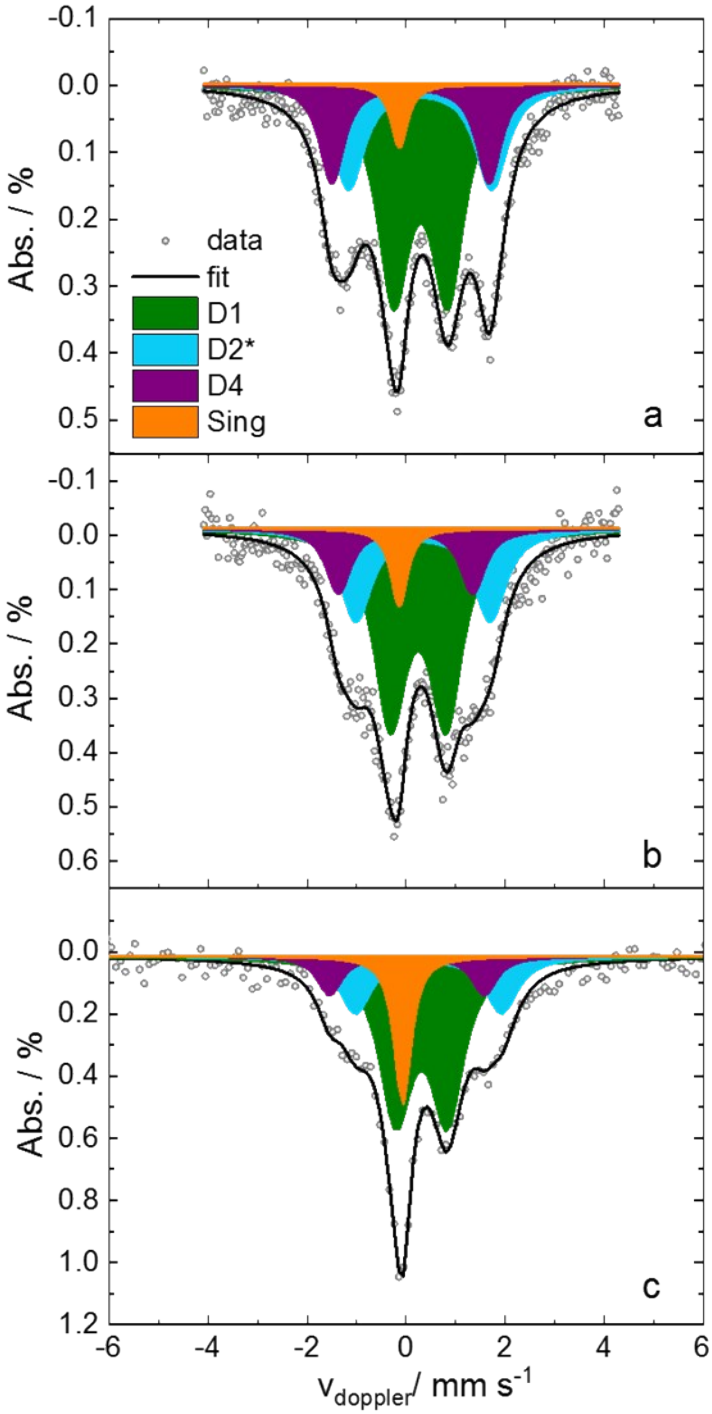

Figure S17: Deconvoluted Mössbauer spectra of the porphyrin-based samples synthesized with 2 (a), 54 (b) and 98 % ^{57}Fe-enrichment (c).

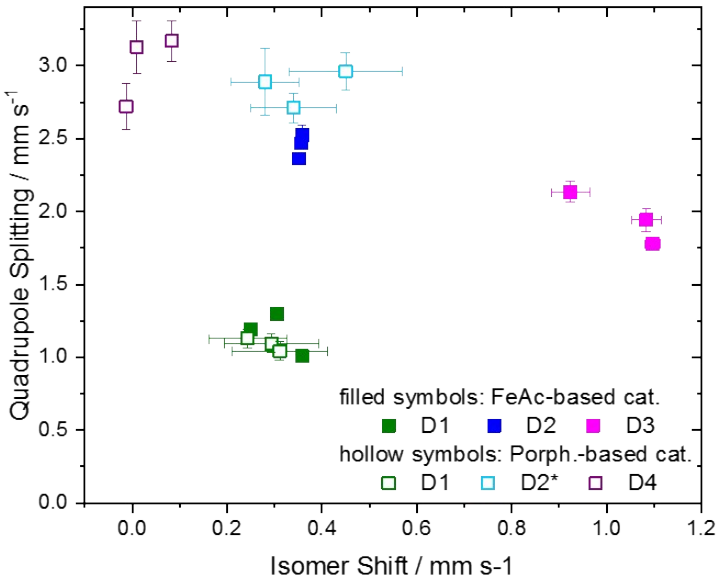

Figure S18: Relation between the Mössbauer doublets' isomer shift and quadrupole splitting values for all the catalysts included in this study.

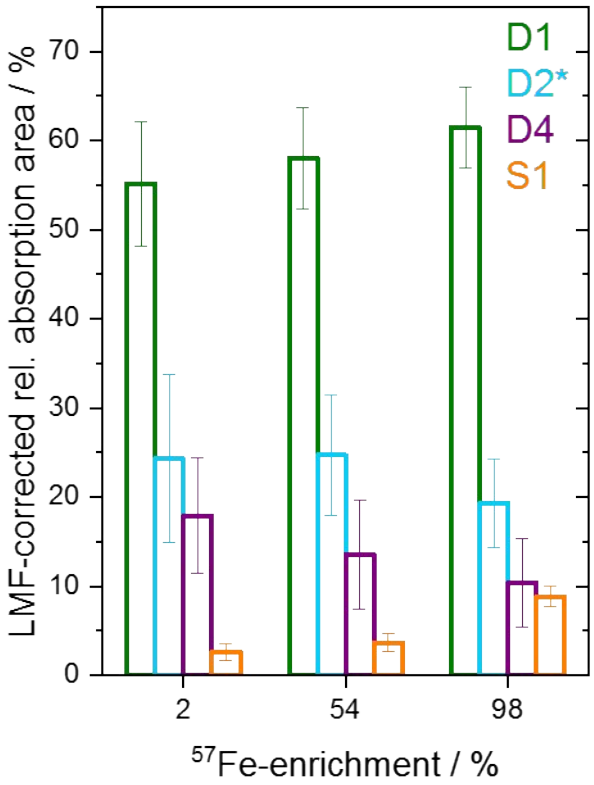

Figure S19: Effect of the degree of ^{57}Fe-enrichment of the three porphyrin-based catalysts on their LMF-corrected relative MS absorption areas for the doublets assigned to Fe-N_x-sites (D1, D2* and D4) and the singlet assigned to superparamagnetic iron (S1).

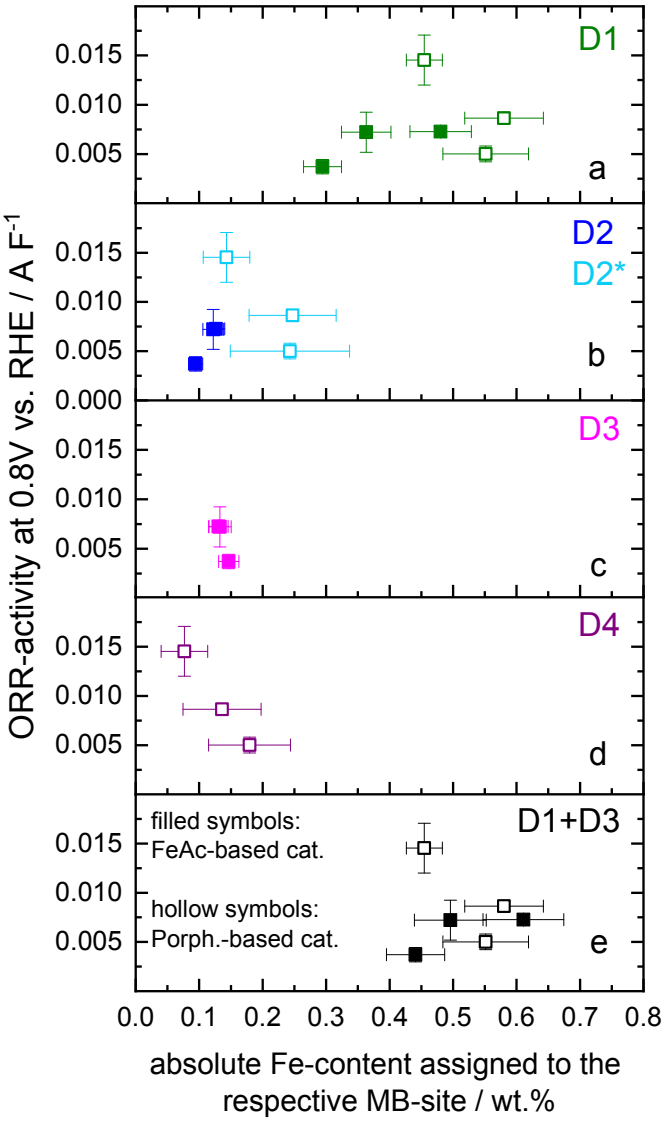

Figure S20: ORR-activity at 0.8 V vs. RHE normalized by the catalyst mass-specific capacitance of the respective catalysts as a function of the absolute Fe-content assigned to the D1 (a), D2 or D2* (b), D3 (c), D4 (d) and cumulative D1 and D3 (e) sites derived from the deconvoluted MS spectra of all catalysts included in this study. The filled symbols refer to catalysts prepared with the FeAc-based approach, while hollow symbols represent the Fe-porphyrin based materials.In this analysis, only the MS-doublets were considered since they have been assigned to atomically dispersed sites of the Fe-N_x-type, which are widely agreed to be the active sites in these materials[12,19,24–28] Furthermore, the cumulative Fe-content in D1 and D3 sites is also addressed, since previous findings have concluded that these two species constitute the main ORR-activity contributors.[18,19,29,30] Lastly it should be noted that this activity-composition assessment is conducted on the basis of the ORR kinetic current normalized by the capacitance to account for the influence of the ≈ 1 order of magnitude different mass-normalized double layer capacitances (assumed to be proportional to the electrochemical surface areas) displayed by the two catalyst series (amounting to ≈ 280 vs. ≈ 40 $F \cdot g^{-1}$ for the FeAc- vs. Fe-porphyrin based samples, respectively).

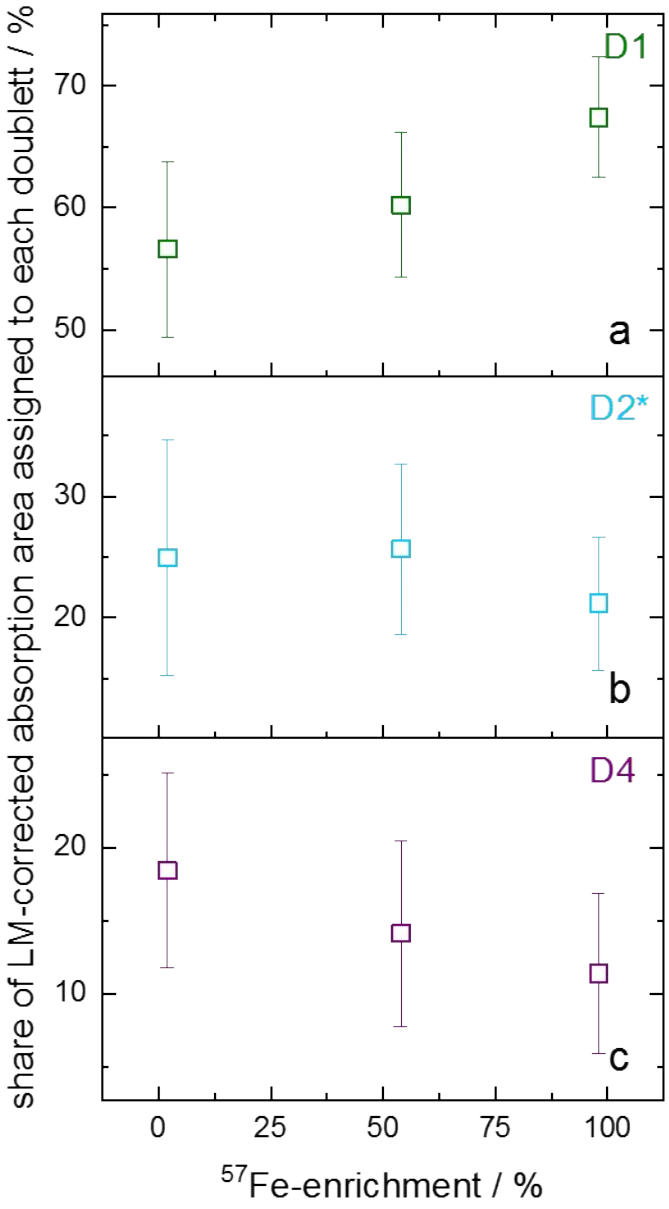

Figure S21: D1 (a), D2*(b) and D4 (c) site's share of the total LMF-corrected absorption area in the deconvoluted MS-spectra for the porphyrin-based catalysts series assigned to Fe-N_x-sites (i.e., all Mössbauer doublets).

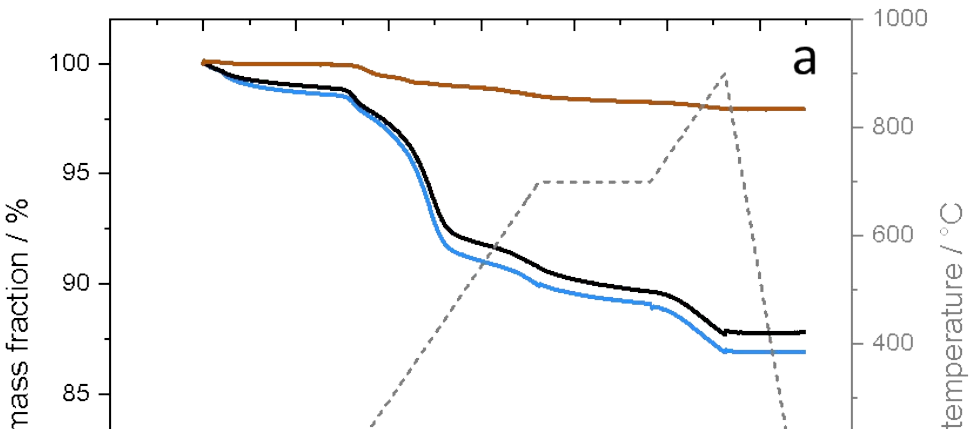

References

1 K. Ebner, J. Herranz, V. A. Saveleva, B. Kim, S. Henning, M. Demicheli, F. Krumeich, M. Nachtegaal and T. J. Schmidt, *ACS Appl. Energy Mater.*, 2019, **2**, 1469–1479.

2 A. F. Holleman, N. Wiberg and E. Wiberg, *Lehrbuch der Anorganischen Chemie*, Walter de Gruyter & Co., Berlin, 102nd edn., 2008.

3 U. I. Kramm, I. Abs-Wurmbach, I. Herrmann-Geppert, J. Radnik, S. Fiechter and P. Bogdanoff, *J. Electrochem. Soc.*, 2011, **158**, B69–B78.

4 T. J. Schmidt, H.A. Gasteiger, G. D. Stäb, D. M. Kolb and R. J. Behm, *J. Electrochem. Soc.*, 1998, **145**, 2354–2358.

5 F. Jaouen, J. Herranz, M. Lefevre, J. P. Dodelet, U. I. Kramm, I. Herrmann, P. Bogdanoff, J. Maruyama, T. Nagaoka, A. Garsuch, J. R. Dahn, T. Olson, S. Pylypenko, P. Atanassov and E. A. Ustinov, *ACS Appl. Mater. Interfaces*, 2009, **1**, 1623–1639.

6 F. Krumeich, E. Müller, R. A. Wepf and R. Nesper, *J. Phys. Chem. C*, 2011, **115**, 1080–1083.

7 O. Müller, M. Nachtegaal, J. Just, D. Lützenkirchen-Hecht and R. Frahm, *J. Synchrotron Radiat.*, 2016, **23**, 260–266.

8 A. H. Clark, P. Steiger, B. Bornmann, S. Hitz, R. Frahm, D. Ferri and M. Nachtegaal, *J. Synchrotron Radiat.*, 2020, **27**, 681–688.

9 B. Ravel and M. Newville, *J. Synchrotron Radiat.*, 2005, **12**, 537–541.

10 A. H. Clark, J. Imbao, R. Frahm and M. Nachtegaal, *J. Synchrotron Radiat.*, 2020, **27**, 551–557.

11 M. Newville, XAFS Spectra Library, http://cars.uchicago.edu/xaslib/spectrum/729, (accessed 8 June 2017).

12 A. Zitolo, V. Goellner, V. Armel, M.-T. Sougrati, T. Mineva, L. Stievano, E. Fonda and F. Jaouen, *Nat. Mater.*, 2015, **14**, 937–42.

13 V. Goellner, V. Armel, A. Zitolo, E. Fonda and F. Jaouen, *J. Electrochem. Soc.*, 2015, **162**, H403–H414.

14 FIZ Karlsruhe, ICSD database, https://icsd.fiz-karlsruhe.de/search/basic.xhtml, (accessed 21 November 2018).

15 B. Ravel, *J. Synchrotron Radiat.*, 2015, **22**, 1258–1262.

16 M. T. Sougrati, V. Goellner, A. K. Schuppert, L. Stievano and F. Jaouen, *Catal. Today*, 2016, **262**, 110–120.

17 G. Gouadec and P. Colomban, *Prog. Cryst. Growth Charact. Mater.*, 2007, **53**, 1–56.

18 U. I. Kramm, M. Lefèvre, N. Larouche, D. Schmeisser and J.-P. Dodelet, *J. Am. Chem. Soc.*, 2014, **136**, 978–985.

19 U. I. Kramm, J. Herranz, N. Larouche, T. M. Arruda, M. Lefèvre, F. Jaouen, P. Bogdanoff, S. Fiechter, I. Abs-Wurmbach, S. Mukerjee and J.-P. Dodelet, *Phys. Chem. Chem. Phys.*, 2012, **14**, 11673–88.

20 F. Tuinstra and J. L. Koenig, *J. Chem. Phys.*, 1970, **53**, 1126–1130.

21 A. C. Ferrari, J. C. Meyer, V. Scardaci, C. Casiraghi, M. Lazzeri, F. Mauri, S. Piscanec, D. Jiang, K. S. Novoselov, S. Roth and A. K. Geim, *Phys. Rev. Lett.*, 2006, **97**, 187401.

22 A. Sadezky, H. Muckenhuber, H. Grothe, R. Niessner and U. Pöschl, *Carbon N. Y.*, 2005, **43**, 1731–1742.

23 M. Newville, *FEFFIT - Using FEFF to model XAFS data*, Chicago, 1998.

24 H. T. Chung, D. A. Cullen, D. Higgins, B. T. Sneed, E. F. Holby, K. L. More and P. Zelenay, *Science (80-.).*, 2017, **357**, 479–484.

25 H. Fei, J. Dong, Y. Feng, C. S. Allen, C. Wan, B. Volosskiy, M. Li, Z. Zhao, Y. Wang, H. Sun, P. An, W. Chen, Z. Guo, C. Lee, D. Chen, I. Shakir, M. Liu, T. Hu, Y. Li, A. I. Kirkland, X. Duan and Y. Huang, *Nat. Catal.*, 2018, **1**, 63–72.

26 J. Li, S. Ghoshal, W. Liang, M. T. Sougrati, F. Jaouen, B. Halevi, S. McKinney, G. McCool, C. Ma, X. Yuan, Z. F. Ma, S. Mukerjee and Q. Jia, *Energy Environ. Sci.*, 2016, **9**, 2418–2432.

27 U. I. Kramm, I. Herrmann-Geppert, S. Fiechter, G. Zehl, I. Zizak, I. Dorbandt, D. Schmeißer and P. Bogdanoff, *J. Mater. Chem. A*, 2014, **2**, 2663–2670.

28 C. H. Choi, C. Baldizzone, G. Polymeros, E. Pizzutilo, O. Kasian, A. K. Schuppert, N. Ranjbar Sahraie, M. T. Sougrati, K. J. J. Mayrhofer and F. Jaouen, *ACS Catal.*, 2016, **6**, 3136–3146.

29 C. E. Szakacs, M. Lefevre, U. I. Kramm, J.-P. P. Dodelet and F. Vidal, *Phys. Chem. Chem. Phys.*, 2014, **16**, 13654–13661.

30 Q. Jia, N. Ramaswamy, H. Hafiz, U. Tylus, K. Strickland, G. Wu, B. Barbiellini, A. Bansil, E. F. Holby, P. Zelenay and S. Mukerjee, *ACS Nano*, 2015, **9**, 12496–12505.